JOURNAL OF PROPULSION AND POWER
Vol. 29, No. 2, March–April 2013

Numerical Analysis of Hybrid Rocket Combustion

Andrea Coronetti* and William A. Sirignano†
University of California, Irvine, California 92697

DOI: 10.2514/1.B34760

Hybrid rocket combustion has important effects on rocket performance. The solid fuel regression rate is an important quantity in the hybrid rocket operation. In the past years, experimental and analytical investigations have been conducted to find correlations to correctly predict the regression rate. Numerical computations are becoming more important in the estimation of the characteristic parameters of such a complex combustion that embraces many different phenomena. This study predicts the regression rate of the Hydroxyl-Terminated Poly-Butadiene/Gaseous Oxygen formulation and its sensitivities to some operating parameters, such as combustion chamber pressure, oxygen inlet temperature, and mass flow rate. Furthermore, an analysis of other variables is used to explain the experimentally observed regression rate behavior. Particular emphasis is placed on the effect of the oxygen between the flame and the surface, which is considered responsible for the pyrolysis process enhancement.

Nomenclature

A	=	pre-exponential coefficient for Arrhenius law, $m^{3(or-1)} \cdot kmol^{-(or-1)} \cdot s^{-1}$
a	=	absorptivity
b	=	Arrhenius law temperature exponent
B_{td}	=	pre-exponential coefficient for pyrolysis law, $mm \cdot s^{-1}$
C	=	specific heat, $J \cdot kg^{-1} \cdot K^{-1}$
c	=	mixture fraction
C_c	=	scalar variance model closure coefficient
C_{C_1}	=	scalar variance model closure coefficient
C'_{C_1}	=	scalar variance model closure coefficient
C_{D_1}	=	scalar variance model closure coefficient
C_{D_2}	=	scalar variance model closure coefficient
C_M	=	molar concentration, $kmol \cdot m^{-3}$
C_{P_1}	=	scalar variance model closure coefficient
$C_{\epsilon 1}$	=	k-ϵ model closure coefficient
$C_{\epsilon 2}$	=	k-ϵ model closure coefficient
C_μ	=	constant of k-ϵ model
D	=	diffusivity, $m^2 \cdot s^{-1}$
E	=	activation energy, $J \cdot kmol^{-1}$
G	=	incident radiation, $W \cdot m^{-2}$
G_{ox}	=	oxygen mass velocity, $kg \cdot m^{-2} \cdot s^{-1}$
h	=	sensible enthalphy, $J \cdot kg^{-1}$
h_f	=	enthalphy of formation, $J \cdot kg^{-1}$
h_t	=	total enthalphy, $J \cdot kg^{-1}$
K	=	thermal conductivity, $W \cdot m^{-1} \cdot K^{-1}$
k	=	turbulent kinetic energy, $m^2 \cdot s^{-2}$
Le	=	Lewis number
$\dot{m}$	=	mass flow rate, $kg \cdot s^{-1}$
N_P	=	combustion products number
N_R	=	reactions number
N_S	=	species number
or	=	reaction order
p	=	pressure, atm
Pr	=	Prandtl number
q	=	thermal flux, $W \cdot m^{-2}$
Q	=	heat source, $W \cdot m^{-3}$
$\dot{r}$	=	regression rate, $mm \cdot s^{-1}$
R	=	universal gas constant, $J \cdot kg^{-1} \cdot K^{-1}$
Re	=	Reynolds number
RR	=	reaction rate, $kmol \cdot m^{-3} \cdot s^{-1}$
S	=	area, m^2
Sc	=	Schmidt number
T	=	temperature, K
t	=	time, s
u	=	velocity component, $m \cdot s^{-1}$
Y	=	mass fraction
α	=	mixture ratio
Γ	=	radiation model coefficient
δ	=	Kronecker's delta
ϵ	=	turbulent eddy dissipation, $m^2 \cdot s^{-3}$
ϵ_c	=	scalar variance dissipation, s^{-1}
ϵ_s	=	emissivity
κ	=	partially stirred reactor coefficient
μ	=	molecular viscosity, $Pa \cdot s$
ν	=	stoichiometric coefficient
ρ	=	density, $kg \cdot m^{-3}$
σ	=	Stefan–Boltzmann constant, $W \cdot m^{-2} \cdot K^{-4}$
σ_k	=	k-ϵ model closure coefficient
σ_ϵ	=	k-ϵ model closure coefficient
τ	=	viscous stress, Pa
τ_c	=	chemical time, s
τ_{mix}	=	turbulent mixing time, s
φ	=	Shvab–Zeldovich variable
ϕ	=	stoichiometric mixture ratio
$\dot{\omega}$	=	source/sink

Subscripts

C_4H_6	=	1.3-Butadiene
CO	=	carbon monoxide
CO_2	=	carbon dioxide
D	=	diameter
exp	=	experimental
F	=	flame
f	=	fuel
g	=	gas
H_2O	=	water
in	=	inlet
L	=	length
mix	=	mixing
num	=	numerical
ox	=	oxygen
O_2	=	oxygen
rad	=	radiation
s	=	solid
t	=	turbulent

Received 12 August 2012; revision received 23 October 2012; accepted for publication 26 October 2012; published online 20 February 2013.

*Visiting Researcher, Department of Mechanical and Aerospace Engineering.

†Professor, Department of Mechanical and Aerospace Engineering. AIAA Fellow.

Introduction

HYBRID rockets have been a scarcely studied technology for decades, but interest has grown in the last decade. Alongside solid and liquid rockets, hybrid rockets belong to the chemical propulsion family, but the hybrid is different from the other two, which have been largely studied and tested with several practical applications. The hybrid rocket is not a candidate for orbital launches, but for suborbital launches only. This technology has been conceptualized to have the advantages of the other two chemical propulsion types, such as flexibility during functioning, multiple ignitions, construction simplicity, and cost reduction. Usually, these advantages are counterbalanced by great drawbacks that are responsible for the poor practical development of this technology, e.g., low regression rate, which means low thrust levels, and poor combustion efficiency because of the poor diffusion on a macroscopic scale, which produces much unburnt fuel, an issue usually solved using postcombustion chambers; other minor issues are the combustion instabilities, which yield to the rough combustion and the mixture ratio shifting [1,2].

The solid fuel regression rate represents the most important design parameter for a hybrid rocket. This parameter has been largely investigated, exploiting experimental apparatus and analytical models to describe its behavior, usually correlating it to operating parameters such as the mass flow rate and the combustion chamber pressure. The first analytical model was developed by Marxman and Wooldridge [3] and Marxman and Gilbert [4] in the 1960s, based on an analysis of the turbulent boundary layer with a diffusion-limited combustion process, including the radiative effects. In this analysis, the regression rate was found to be a function of the oxygen mass velocity G_{ox} with a power law dependency, whereas other operating conditions were not considered to affect the regression rate estimation.

Some years later, Price and Smoot [5,6] were the first to theorize the possible pressure dependency of the regression rate, observing how the exponent of G_{ox} varied due to the change in the operating conditions, and not only due to change in mass flow rate. They sought a theoretical explanation for such behavior, particularly addressing this sensitivity to the enhancement in solid fuel pyrolysis, through heterogeneous reactions due to the presence of oxygen below the diffusion flame. Pressure sensitivity was also observed to increase as the mass flow rate increases.

No more remarkable studies were conducted until the 1990s, when some experimental analyses on fuel pyrolysis were conducted by Arisawa and Brill [7,8] and by Risha et al. [9]. Arisawa and Brill [7,8] considered the pressure effect on particular pyrolysis properties; they found that the pyrolysis process was dominated by the matrix decomposition at a lower temperature, whereas it was dominated by the rate of desorption at a higher temperature. The transition temperature between the two governing phenomena was found to be pressure sensitive. Risha et al. [9] found an inverse pressure dependency on regression rate. They also proposed an empirical law to account for many operating conditions affecting the regression rate:

$$\dot{r} = 3.02(Y_{O_2} - 0.21)^{0.19} T_{ox}^{1.28} \frac{\dot{m}_{ox}^{0.5}}{p^{0.43}} \tag{1}$$

Equation (1) shows a sensitivity not only to mass flow rate and pressure, but also to oxygen inlet temperature and freestream oxygen mass fraction. Also in this case, the presence of oxygen below the flame was assumed to affect the regression rate behavior, and is explained with the following factors: the absorption of oxygen at the solid grain surface, exothermic heterogeneous reactions at the surface, and enhanced heat transfer toward the surface due to the homogeneous reactions between oxygen and pyrolysis products.

A new analytical model to evaluate the pressure sensitivity to regression rate has been recently proposed by Favarò et al. [10]. The model analyzed the turbulent boundary layer and the diffusion flame to evaluate the causes for the experimentally observed regression rate behavior. The problem has been studied assuming a uniform regression rate along the grain surface, fast-chemistry hypothesis, and neglecting transverse and streamwise diffusions. Initially, profiles for temperature, oxygen, and fuel mass fractions in the boundary layer were obtained; then, they were used in two approaches: the first one imposed matching conditions at the flame and at the surface, and the second one was based on a conserved scalar approach. In both cases, the analytical scheme provided seven equations with seven unknowns that were numerically solved. The results, assuming decreasing regression rate with increasing pressure, agreed with those of Risha et al. [9]. The experimental results obtained at Politecnico di Milano [10] have also been used as initial data for the numerical computations, and the authors proposed a semi-empirical law for the regression rate estimation:

$$\dot{r} = A[c + (\rho_s Y_{ox_s})^n] \exp\left(-\frac{E_1}{T_s}\right) - B \exp\left(-\frac{E_2}{T_s}\right) - C(\rho_s Y_{f_s}) \tag{2}$$

where all of the coefficients have been obtained through fitting.

However, hybrid rocket combustion involves many concurrent phenomena taking place in the combustion chamber that differ in physical nature and behaviors. An analytical model that uses all of the aspects would not be solved easily. For this reason, and because of the improvement in the computing assets in the last decade, the numerical solutions are possibly preferable. Examples of these studies can be found in the analyses by Zilliac and Karabeyoglu [11] and Gariani et al. [12]. The first analysis started from the analytical model of Marxman [3,4], and pointed out the importance of a good description of the thermal flux imbalance at the surface, which accounted for all of the main phenomena affecting the surface temperature, such as convection, radiation, and pyrolysis. Zilliac and Karabeyoglu [11] also proposed a regression rate correlation with dependencies on G_{ox}, port diameter, grain length, fuel thermophysical characteristics, flow characteristics, and surface temperature. The second work [12] used OpenFOAM [13] to make simulations of the hybrid rocket combustion at low pressure, simulating an experimental combustion chamber flow, using the Reynolds-averagedFF Navier-Stokes equation and a chemical kinetics scheme and providing analysis on the mass flow rate and pressure dependencies.

Analytical Modeling

The analytical model used for the numerical analysis is presented in the present paper. This model takes into account the solution in the fluid flow, which is schematically a circular channel, surrounded by a solid grain, representing the fuel, which is solved as well. The solution in the fluid flow is more complex because it involves many different phenomena and properties that can affect the solution, whereas for the solid domain, only the temperature profile can be considered. The two domains are strictly connected by another physical phenomenon, i.e., the fuel pyrolysis that converts the solid fuel in vapors entering the fluid flow. The analysis reported in this paper will focus on the combustion of Hydroxyl-Terminated Poly-Butadiene (HTPB), as fuel, fed by gaseous oxygen.

Reacting Flow Model

Fluid flows can be generally described relying on the Navier–Stokes equations; however, for the numerical computations, there are many techniques to solve these types of equations. In this work, the solution is obtained through the Favre-averaged Navier–Stokes equations reported:

Continuity equation:

$$\frac{\partial \bar{\rho}}{\partial t} + \frac{\partial \bar{\rho} \tilde{u}_j}{\partial x_j} = 0 \tag{3}$$

Momentum equation:

$$\frac{\partial \bar{\rho} \tilde{u}_i}{\partial t} + \frac{\partial \bar{\rho} \tilde{u}_i \tilde{u}_j}{\partial x_j} = -\frac{\partial \bar{p}}{\partial x_i} + \frac{\partial \bar{\tau}_{ij}}{\partial x_j} - \frac{\partial \overline{\rho u_i'' u_j''}}{\partial x_j} \tag{4}$$

Energy equation:

$$\frac{\partial \bar{\rho}\tilde{h}_t}{\partial t} + \frac{\partial \bar{\rho}\tilde{h}_t\tilde{u}_j}{\partial x_j} = \frac{\partial \bar{p}}{\partial t} + \frac{\partial}{\partial x_j}\left(\bar{\rho}\alpha\frac{\partial \tilde{h}}{\partial x_j} + \tilde{u}_i\bar{\tau}_{ij}\right) + \bar{\dot{Q}}_{\text{rad}} + \sum_{k=1}^{N_s}\bar{\rho}\, h_{f_k}\bar{\dot{\omega}}_k - \frac{\partial\overline{\rho h_t'' u_j''}}{\partial x_j} \tag{5}$$

Species conservation equation:

$$\frac{\partial \bar{\rho}\tilde{Y}_k}{\partial t} + \frac{\partial \bar{\rho}\tilde{Y}_k\tilde{u}_i}{\partial x_j} = \frac{\partial}{\partial x_j}\left(\bar{\rho}D_k\frac{\partial \tilde{Y}_k}{\partial x_j}\right) + \bar{\dot{\omega}}_k - \frac{\partial\overline{\rho Y_k'' u_j''}}{\partial x_j} \tag{6}$$

In a reacting flow, the energy and species conservation equations are coupled with the solution for the continuity and momentum equation, because density can largely vary in the flow due to the reactions and the amount of heat injected in the flow. The equations are written for the more general case of unsteady and compressible flow, because the solution is analyzed starting from the rocket ignition, which is an unsteady phase, and progresses until a steady-state condition. The Favre-averaging procedure introduces another kind of stress, alongside the viscous stress, represented by τ_{ij}, which is the Reynolds stress due to turbulence, represented by averaging the fluctuation terms, which are stresses in the momentum equation and fluxes in the energy and species conservation equations. None of these terms can be solved without modeling, which usually uses a turbulence closure model. In this work, the k-ϵ model is used to close the problem, and assuming the hypothesis that $Pr = Le = Sc = 1$, so that the thermal diffusivity and the mass diffusivities are equal to the viscosity, only the turbulent viscosity is computed:

$$\mu_t = C_\mu\bar{\rho}\frac{k^2}{\epsilon} \tag{7}$$

Hence, the correlations can be expressed as

$$-\overline{\rho u_i'' u_j''} = \mu_t\left(\frac{\partial \tilde{u}_i}{\partial x_j} + \frac{\partial \tilde{u}_j}{\partial x_i} - \frac{2}{3}\delta_{ij}\tilde{k}\right) \tag{8}$$

$$-\overline{\rho T'' u_j''} = \mu_t\frac{\partial \tilde{T}}{\partial x_j} \tag{9}$$

$$-\overline{\rho Y_k'' u_j''} = \mu_t\frac{\partial \tilde{Y}_k}{\partial x_j} \tag{10}$$

Turbulent kinetic energy k and its dissipation ϵ can be solved using the two model equations for the unsteady-compressible case with Favre averaging:

Turbulent kinetic energy transport equation:

$$\frac{\partial \bar{\rho}\,\tilde{k}}{\partial t} + \frac{\partial \bar{\rho}\,\tilde{k}\,\tilde{u}_j}{\partial x_j} = \frac{\partial}{\partial x_j}\left[\left(\mu + \frac{\mu_t}{\sigma_k}\right)\frac{\partial \tilde{k}}{\partial x_j}\right] + \mu_t\left(\frac{\partial \tilde{u}_j}{\partial x_j}\right)^2 - \bar{\rho}\epsilon \tag{11}$$

Turbulent eddy dissipation equation:

$$\frac{\partial \bar{\rho}\epsilon}{\partial t} + \frac{\partial \bar{\rho}\epsilon\tilde{u}_j}{\partial x_j} = \frac{\partial}{\partial x_j}\left[\left(\mu + \frac{\mu_t}{\sigma_\epsilon}\right)\frac{\partial \epsilon}{\partial x_j}\right] + C_{\epsilon 1}\mu_t\frac{\epsilon}{k}\left(\frac{\partial \tilde{u}_j}{\partial x_j}\right)^2 - C_{\epsilon 2}\bar{\rho}\frac{\epsilon^2}{k} \tag{12}$$

The recommended values for the constants in the two equations are [14] $\sigma_k = 1$, $\sigma_\epsilon = 1.3$, $C_{\epsilon 1} = 1.44$, and $C_{\epsilon 2} = 1.92$.

Alternatively, the turbulence closure model can use more complex relations; in fact, the k-ϵ model provides a mixing defined by the momentum only. However, because of the nature of the mixing between fuel and oxidizer, a variable that better describes this mixing would be useful. The mixture fraction c is a suitable variable to describe this mixing, and is defined as follows:

$$c = \frac{\varphi - \varphi_0}{\varphi_1 - \varphi_0} \tag{13}$$

where φ is defined as

$$\varphi = Y_f - \frac{Y_{\text{ox}}}{\phi} \tag{14}$$

This Eq. (14) defines a relation between the amount of oxygen and fuel starting from their stoichiometric value ϕ, which is set to 2.7, according to Zilliac and Karabeyoglu [11].

A general transport equation can be written for the scalar variable c ($Sc = 1$):

$$\rho\frac{\partial c}{\partial t} + \rho u_j\frac{\partial c}{\partial x_j} = \frac{\partial}{\partial x_j}\left(\mu\frac{\partial c}{\partial x_j}\right) \tag{15}$$

Starting from this equation, it is necessary to obtain equations for the scalar fluctuation variance and its dissipation. Elghobashi and Launder [15] derived these equations for the incompressible, steady-state case, neglecting viscous stresses for the scalar temperature, alongside a third equation for the correlation between velocity and scalar fluctuations. Jones and Whitelaw [16] derived only the scalar variance equation for the compressible, steady-state case for the scalar mixture fraction. In this work, the equations have been derived in the compressible, unsteady case with viscous effects applying the Favre averaging to the scalar and momentum equations.

The Favre-averaged mixture fraction equation becomes

$$\frac{\partial \bar{\rho}\,\tilde{c}}{\partial t} + \frac{\partial \bar{\rho}\tilde{u}_j\tilde{c}}{\partial x_j} = \frac{\partial}{\partial x_j}\left(\mu\frac{\partial \tilde{c}}{\partial x_j}\right) - \overline{\rho\frac{\partial u_j'' c''}{\partial x_j}} \tag{16}$$

The scalar variance equation for $\overline{\rho c'' c''}$ can be derived by multiplying Eq. (15) by $2\,c''$ and averaging over time. With other simplifications, we get

$$\overline{\rho\frac{\partial c'' c''}{\partial t}} + \tilde{u}_j\overline{\rho\frac{\partial c'' c''}{\partial x_j}} = \overline{\frac{\partial}{\partial x_j}\left(\mu\frac{\partial c'' c''}{\partial x_j}\right)} - \overline{\rho\frac{\partial u_j'' c'' c''}{\partial x_j}} - 2\overline{\rho u_j'' c''}\frac{\partial \tilde{c}}{\partial x_j} - 2\mu\overline{\frac{\partial c''}{\partial x_j}\frac{\partial c''}{\partial x_j}} \tag{17}$$

In this equation, the terms on the left-hand side are the time derivative and advection terms; the first term on the right-hand side accounts for the viscous effects, the second term is a triple correlation term representing the turbulent diffusion, the third term is the production rate of $\overline{\rho c'' c''}$, and the last term is the dissipation, which can be expressed as $\bar{\rho}\epsilon_c$. The modeling for this equation is provided by Elghobashi and Launder [15]; the triple correlation term can be expressed as

$$-\overline{\rho\frac{\partial \overline{u_j'' c'' c''}}{\partial x_j}} = -C_c\overline{\rho u_i'' u_j''}\,\tau_{\text{mix-c}}\frac{\partial \overline{c'' c''}}{\partial x_j} \tag{18}$$

where C_c is a model coefficient equal to 0.35 [15], $\overline{\rho u_i'' u_j''}$ can be expressed as Eq. (8), and $\tau_{\text{mix-}c}$ is the mixing time calculated with the scalar variance and its dissipation:

$$\tau_{\text{mix-c}} = \frac{1}{2}\frac{\overline{c'' c''}}{\epsilon_c} \tag{19}$$

The equation for ϵ_c can be easily written as follows:

$$\overline{\rho\frac{\partial \epsilon_c}{\partial t}} + \tilde{u}_j\overline{\rho\frac{\partial \epsilon_c}{\partial x_j}} = \overline{\frac{\partial}{\partial x_j}\left(\mu\frac{\partial \epsilon_c}{\partial x_j}\right)} - \overline{\rho\frac{\partial u_j'' \epsilon_c}{\partial x_j}} - C_{P_1}\frac{\epsilon_c}{\overline{c^2}}\overline{\rho u_j'' c''}\frac{\partial \tilde{c}}{\partial x_j} - \rho\epsilon_c s\left(C_{D_1}\frac{\epsilon_c}{\overline{c^2}} + C_{D_2}\frac{\epsilon}{k}\right) \tag{20}$$

The first three terms are the time derivative, advection, and viscous contribution for ϵ_c. The second term on the right-hand side needs to be modeled, and this is done in a similar way as for the scalar variance:

$$-\overline{\rho\frac{\partial u_j''\epsilon_c}{\partial x_j}} = -C_c\overline{\rho u_i''u_j''}\tau_{\text{mix-c}}\frac{\partial \epsilon_c}{\partial x_j} \tag{21}$$

The third term is the production term, which is the same term that appears in Eq. (17), multiplied by the coefficient $C_{P_1}\frac{\epsilon_c}{\overline{c''c''}}$, where C_{P_1} is a model coefficient equal to 1.8 [15]. The last term in the ϵ_c transport equation is the destruction term, which involves the dissipation itself, but its contribution is produced by two effects, one related to the scalar mixing and the other to the momentum mixing. The constants C_{D_1} and C_{D_2} are, respectively, 2.2 and 0.8 [15].

The transport equation for $\overline{\rho u_i''c''}$ is derived through the following steps:

1) Multiply the momentum equation by c''.
2) Multiply the scalar transport equation by u_i''.
3) Time-average both equations.
4) Sum the two equations.

The resulting equation is

$$\begin{aligned}\overline{\rho\frac{\partial u_i''c''}{\partial t}} + \tilde{u}_j\overline{\rho\frac{\partial u_i''c''}{\partial x_j}} &= \overline{\frac{\partial}{\partial x_j}\left(\mu\frac{\partial u_i''c''}{\partial x_j}\right)} - \overline{\rho\frac{\partial u_i''u_j''c''}{\partial x_j}} \\ &- \overline{\rho c''u_j''}\frac{\partial \tilde{u}_i}{\partial x_j} - \overline{\rho u_i''u_j''}\frac{\partial \tilde{c}}{\partial x_j} - \frac{\partial(\overline{p'c''})}{\partial x_i} \\ &+ \overline{\frac{\partial c''}{\partial x_i}p'} - 2\mu\overline{\frac{\partial u_j''}{\partial x_j}\frac{\partial c''}{\partial x_j}}\end{aligned} \tag{22}$$

Again, the first three terms are the time derivative, advection, and viscous contribution for $\overline{\rho u_i''c''}$. The triple correlation term can be modeled in analogy with what has been done for scalar variance:

$$-\overline{\rho\frac{\partial u_i''u_j''c''}{\partial x_j}} = -C_c\overline{\rho u_i''u_j''}\tau_{\text{mix-c}}\frac{\partial\overline{u_j''c''}}{\partial x_j} \tag{23}$$

The first two terms on the second line of Eq. (22) are the two production terms. The next two terms are the pressure scalar correlations; the first one is very small if compared with the other terms representing turbulent and molecular diffusions. Therefore, it is neglected. The second term represents the redistribution of $\overline{\rho u_i''c''}$ due to the interaction between pressure fluctuations and scalar gradient, and it is modeled as follows:

$$\overline{\frac{\partial c''}{\partial x_j}p'} = -\left[C_{c1}\overline{\rho u_i''c''} + C'_{c1}\overline{\rho u_i''c''}\left(\overline{u_i''u_j''} - \frac{2}{3}k\delta_{ij}\right)\frac{1}{k}\right]\frac{1}{\tau_{\text{mix-c}}} \tag{24}$$

where C_{c1} and C'_{c1} are closure coefficients, and their values are, respectively, 2.15 and −1.6 [15], whereas k is the turbulent kinetic energy.

Finally, the last term is a destruction term, and observing the structure of the turbulent kinetic energy dissipation ϵ and the scalar variance dissipation ϵ_c, one can assume that the dissipation for $\overline{\rho u_i''c''}$ can be expressed as a function of the other two dissipations:

$$\mu\overline{\frac{\partial u_i''}{\partial x_j}\frac{\partial c''}{\partial x_j}} = \bar{\rho}\sqrt{\epsilon\epsilon_c} \tag{25}$$

Chemical Kinetics Scheme

In this work, the chemistry is solved by integrating the chemical kinetics, hence using a finite rate chemistry model. From the experimental measurements of pyrolysis by Risha et al. [9], it is possible to find that 1.3-Butadiene (C_4H_6) is the most common fuel vapor produced by the HTPB pyrolysis in a large temperature range. It can be assumed that the greatest part of oxygen burns with 1.3-Butadiene; hence, a chemical kinetics scheme for the combustion of these two substances is used in this work. This combustion process has been studied by Granata et al. [17] and Goldaniga et al. [18], and a multistep reaction scheme has been provided:

$$C_4H_6 + 2O_2 \rightarrow 4CO + 3H_2 \tag{26}$$

$$C_4H_6 + 4H_2O \rightarrow 4CO + 7H_2 \tag{27}$$

$$CO + H_2O \rightarrow CO_2 + H_2 \tag{28}$$

$$H_2 + \frac{1}{2}O_2 \leftrightarrows H_2O \tag{29}$$

$$O_2 \leftrightarrows 2O \tag{30}$$

$$H_2O \leftrightarrows OH + H \tag{31}$$

The scheme uses six reactions and nine species. Each one of these reactions can be characterized by its reaction rate, which is a measure of the rate of production of the species. This value can be described by means of the Arrhenius law, which is an exponential law describing the reaction rate RR as a nonlinear function of the mixture temperature T. Its general form is as follows:

$$\text{RR}_j = AT^b\ \exp\left(-\frac{E_a}{RT}\right)\prod_{i=1}^{N_r}(C_{M_i})^{\nu'_i} \tag{32}$$

The reported reaction rates of the previous six reactions follow in the same order:

$$\text{RR}_1 = 9.11{*}10^{13}\ \exp\left(-\frac{31200}{RT}\right)(C_4H_6)^{0.5}(O_2)^{1.25} \tag{33}$$

$$\text{RR}_2 = 3.48{*}10^{11}\ \exp\left(-\frac{30600}{RT}\right)(C_4H_6)(H_2O) \tag{34}$$

$$\text{RR}_3 = 2.90{*}10^{12}\ \exp\left(-\frac{19100}{RT}\right)(CO)(H_2O) \tag{35}$$

$$\text{RR}_4 = 2.80{*}10^{18}T^{-1}\ \exp\left(-\frac{43100}{RT}\right)(H_2)^{0.25}(O_2)^{1.5} \tag{36}$$

$$\text{RR}_5 = 1.50{*}10^{9}\ \exp\left(-\frac{113000}{RT}\right)(O_2) \tag{37}$$

$$\text{RR}_6 = 2.30{*}10^{22}T^{-3}\ \exp\left(-\frac{120000}{RT}\right)(H_2O) \tag{38}$$

All of the reaction rates are in kmol $\cdot$ m^{-3} $\cdot$ s^{-1}, whereas activation energies are in cal $\cdot$ mol^{-1}.

Chemistry-Turbulence Interaction

In Eq. (6), the source term $\dot{\omega}_k$ is modeled with a partially stirred reactor (PaSR) model to account for the interaction between chemistry and turbulence. The source term can be expressed as

$$\dot{\omega}_k = \kappa \mathrm{RR}_k \tag{39}$$

where RR_k is the reaction rate for each species; the treatment for the κ coefficient has been studied by Golovitchev et al. [19,20], and can be expressed as

$$\kappa = \frac{\tau_c}{\tau_c + \tau_{\mathrm{mix}}} \tag{40}$$

In this equation, the turbulent mixing time τ_{mix} can be evaluated using either the scalar turbulence properties, i.e., scalar variance $\overline{\rho c'' c''}$ and its dissipation ϵ_c as in Eq. (19), or the momentum turbulence properties, i.e., turbulent kinetic energy k and its dissipation ϵ as follows [21]:

$$\tau_{\mathrm{mix}} = 0.03 \frac{k}{\epsilon} \tag{41}$$

The chemical time to use in the κ relation must be thoroughly discussed. In fact, Golovitchev et al. [19,20] used a chemical time computation that favors the fastest reaction:

$$\tau_c = N_R \frac{\sum_{k=1}^{N_s} C_{M_k}}{\sum j = 1^{N_R} \sum l = 1^{N_P} \nu_{lj}'' \mathrm{RR}_j} \tag{42}$$

where N_S is the number of species, N_R is the number of reactions, N_P is the number of combustion products, (C_M) is the molar density concentration, and ν_{lj}'' is the stoichiometric coefficient of each product l for each reaction j. However, it is usually the slowest reaction, characterized by the longest time, that best describes a multistep reaction mechanism. Calling the smallest chemical time $\tau_{c_{\min}}$ and the largest $\tau_{c_{\max}}$, one can take the following observations related to the relation in Eq. (40):

$$\mathrm{O}(\tau_{\mathrm{mix}})/\mathrm{O}(\tau_{c_{\min}})/\mathrm{O}(\tau_{c_{\max}})$$

In this case, the mixing time is the smallest time in the chemistry-turbulence interaction process, so the value of κ should be equal to 1. The results should be reasonable because the chemistry is rate controlling, but this is the only case in which the model produces acceptable results.

$$\mathrm{O}(\tau_{\mathrm{mix}}) == \mathrm{O}(\tau_{c_{\min}})/\mathrm{O}(\tau_{c_{\max}})$$

In this case, both the mixing and the smallest chemical times are negligible if compared with the largest chemical time; however, with this computation, κ is less than 1, and this reduces the rate by a factor of approximately 2 and doubles the overall time, introducing errors in the estimations because the largest chemical time is still dominant with respect to the mixing one.

$$\mathrm{O}(\tau_{c_{\min}})/\mathrm{O}(\tau_{\mathrm{mix}})/\mathrm{O}(\tau_{c_{\max}})$$

In this condition, the largest chemical time is still dominant if compared with the mixing time, but the κ calculation approach underestimates the conversion rate and overestimates the overall time by orders of magnitude. The prediction yields to an overall conversion time that is much greater than the sum of all the chemical and physical times.

$$\mathrm{O}(\tau_{c_{\min}})/\mathrm{O}(\tau_{\mathrm{mix}}) == \mathrm{O}(\tau_{c_{\max}})$$

In this situation, the sum of the mixing and largest chemical times should determine the magnitude of the overall time for the chemistry-turbulence interaction. However, with the proposed computation, the conversion rate is underestimated and the overall time is overestimated by orders of magnitude. The conclusion is that the predicted overall time is much greater than the sum of all of the chemical and physical times.

$$\mathrm{O}(\tau_{c_{\min}})/\mathrm{O}(\tau_{c_{\max}})/O(\tau_{\mathrm{mix}})$$

In this final case, the mixing time should determine the magnitude of the overall time for the interaction. However, the conversion rate is again underestimated and the overall time is overestimated by orders of magnitude, yielding to a predicted overall time that is much greater than the sum of all of the involved times.

The chemical time proposed by Golovitchev et al. [19,20] is coded in the OpenFOAM source code, which has been used for the numerical computations. The source code has been modified by the authors so that the chemical time calculated is now the longest one:

$$\tau_c = N_R \sum_{j=1}^{N_R} \sum_{l=1}^{N_P} \frac{C_{M_l}}{\nu_{lj}'' \mathrm{RR}_j} \tag{43}$$

Radiation Model

Thermal radiation in the fluid flow is treated with the P-1 model [22,23], which is an approximation of the P-N model that uses harmonic approximation to calculate the incident radiation G. Its diffusion equation is as follows:

$$\nabla \cdot (\Gamma \nabla G) - aG + 4a\sigma T^4 = 0 \tag{44}$$

which is solved using the Marshak radiation boundary condition [22], where a is the absorptivity, σ is the Stefan–Boltzmann constant, and Γ is a coefficient dependent on the absorptivity and the scatter model. The thermal radiation contribution in Eq. (5) is described by the following relation:

$$q_{\mathrm{rad}} = aG - 4a\sigma T^4 \tag{45}$$

Heat Conduction in the Solid Domain

As previously stated, the only important field to analyze in the solid domain is the temperature. The temperature is evaluated by means of a diffusion equation for the solid mean:

$$\frac{\partial}{\partial t}(\rho_s C_s T_s) = \nabla \cdot (K_s \nabla T) \tag{46}$$

In this equation, density, specific heat, and conductivity are assumed to be constant, neglecting their possible dependency with respect to local temperature. This equation is valid in a frame of reference fixed with the surface, which regresses as described later. The thermal inertia term $\dot{r}(\partial T/\partial z)$ is not considered because of its small influence on the solution when the regression rate is far smaller than the mixture velocity ($\dot{r} \ll u_{\mathrm{mix}}$.).

Initial and Boundary Conditions

The analytical model is solved numerically using the open source program OpenFOAM [13], which uses a finite volume discretization. To solve the partial differential equations previously introduced, it is necessary to set proper initial and boundary conditions for each field. The solid domain has a tubular shape, whereas the fluid domain is realized in its port, representing the combustion chamber, and it is extended in both the inlet and outlet directions to avoid numerical problems. Particular boundary conditions are used for the treatment of the fluid-solid interface.

As far as the velocity field is concerned, the channel inlet value is fixed to control the inlet mass flow rate. The no-slip condition is applied along the fluid-solid interface length. However, the turbulent boundary layer of a hybrid rocket is not common because of the wall injection caused by fuel pyrolysis. It is necessary to relate the gas vapor velocity to the solid fuel pyrolysis rate. The computation of the pyrolysis rate must be empirical and is suggested by Risha et al. [9] in the Arrhenius law form, but is modified in the present paper to account for the oxygen at the surface, as follows:

$$\dot{r} = B_{td}(1 + \alpha_{\text{pyr}} Y_{\text{O2}}) \exp\left(-\frac{E_{td}}{RT_s}\right) \tag{47}$$

The values for the pre-exponential coefficient B_{td}, activation energy E_{td}, and pyrolysis mixture fraction α_{pyr} are obtained empirically, and the B_{td} value used by Risha et al. [9] has a pressure dependency. For the continuity at the fluid-solid interface, the wall injection velocity can be evaluated through

$$\rho_s \dot{r} = \rho_g u_{\text{mix}} Y_{\text{ox}} + \rho_g u_{\text{mix}} Y_f - \rho_g D \frac{\partial Y_{\text{ox}}}{\partial n} - \rho_g D \frac{\partial Y_f}{\partial n} \tag{48}$$

This formulation assumes that the gas velocity normal to the surface is much larger than the regression rate, i.e., $u_{\text{mix}} \gg \dot{r}$. On right-hand side of Eq. (48), combustion products advection and diffusion terms are not considered because, for each product, the two terms are equal and opposite, whereas for fuel and oxidizer, they are different, as explained later in the species boundary conditions.

Pressure is an operating condition parameter as is the inlet mass flow rate. Its value is usually fixed in the rocket application, so the values indicated in the analysis are set at the outflow, whereas on the other boundaries, pressure is evaluated ensuring that its normal gradient is zero. Of course, in practice, the pressure can be controlled through the downstream nozzle design.

The temperature field at the inlet is set to 900 K to ensure the mixture ignition without the need of an external thermal source. The fluid temperature at the wall is set to be equal to the solid surface temperature, whose calculation is reported later.

As far as the species mass fractions are concerned, it is necessary to set different boundary conditions for the different species. At the inlet, pure oxygen is injected in the combustion chamber. At the fluid-solid interface, however, not only can the fuel vapors be present, but so can any other species, i.e., combustion products or even oxygen. It is possible to define some velocities, the normal component of the mixture velocity u_{mix}, and a velocity for each species u_i at the interface, which are related through

$$\rho_g u_i = \rho_g u_{\text{mix}} Y_i - \rho_g D \frac{\partial Y_i}{\partial n} \tag{49}$$

For each species, it is possible to write a relation between the species velocity and its source/sink term, as follows:

$$\rho_g u_{\text{mix}} Y_i - \rho_g D \frac{\partial Y_i}{\partial n} = \omega_i \tag{50}$$

which is used to compute the species mass fractions at the fluid-solid interface. The source/sink term ω_i can be evaluated as

$$\omega_i = \mu_i \rho_s \dot{r} \tag{51}$$

The coefficient μ_i can be evaluated according to the species type. Considering that the fuel vapors are not in the same quantity as the fuel solid mass, but the pyrolysis process provides more vapors, μ_f would be expressed as

$$\mu_f = 1 + \alpha_{\text{pyr}} \tag{52}$$

As stated earlier, a small quantity of oxygen (dependent on the value of α_{pyr}) is absorbed inside the solid grain due to pyrolysis processes; this quantity is 0.0014, so the fuel vapors released at the wall are mostly constituted by pure fuel, and only a small and negligible part is composed of oxidized fuel. Thus, oxygen is absorbed at the surface, but its amount is not conserved. Therefore, for μ_{ox}, one can write a negative value as a function of α_{pyr}:

$$\mu_{\text{ox}} = -\alpha_{\text{pyr}} \tag{53}$$

For all of the combustion products produced by the flame, which are not involved in pyrolysis reactions, $\mu_i = 0$.

The solid grain has an initial temperature of 300 K. However, the value at the fluid-solid interface must be updated at every time step and is dependent on many phenomena, such as diffusion in the solid, convection, thermal radiation, and heat released by pyrolysis. Thus, the thermal imbalance can be written as

$$K_g \frac{\partial T}{\partial n} + G_w = K_s \frac{\partial T_s}{\partial n} + \sigma \epsilon_s T_{s_{\text{wall}}}^4 + \rho_s \dot{r} h_{\text{pyr}} \tag{54}$$

The first term represents the conduction, and the gas mixture conductivity K_g is updated as a function of local temperature and turbulence properties; the second term is the incident radiation from flame to surface, calculated with the radiation model; the third term is the diffusion in the solid grain, with constant conductivity; the fourth term is the radiation from the surface to the fluid; and the last term is the heat released by pyrolysis, and the value of the pyrolysis enthalpy is set to 1.1 $\text{MJ} \cdot \text{kg}^{-1}$, according to Ramohalli and Yi [24]. In Eq. (54), the surface temperature appears in a nonlinear fashion; thus, to solve for T_{s_w}, it is necessary to use an interactive cycle.

Moving Interface Treatment

One last physical phenomenon needs to be modeled for the numerical computation: the solid fuel regresses at the same rate at which it burns. This means that the surface regresses in the direction normal to the fluid flow with a velocity equal to the regression rate, which is calculated with Eq. (47). The main consequence is that the fluid-solid interface boundary changes in time, and these modifications are not uniform throughout the grain length but rather vary because at each point the regression rate has a different value; thus, the combustion chamber no longer has a cylindrical shape. The displacement is approximated to occur only in the direction normal to the freestream flow, even though a small displacement could occur in the axial direction, but it is neglected because it involves very small angles. Therefore, all points of the fluid-solid interface are moved according to the local regression rate, and their new positions are automatically updated.

Numerical Results and Comparisons

The numerical analysis provides a thorough description of each variable previously defined, allowing considerations that one cannot obtain only through experiments.

The numerical domain studied in this work has the same size as the experimental apparatus used at the Space Propulsion Laboratory at Politecnico di Milano [10]; therefore, the combustion chamber is realized in the cylindrical port of the solid fuel with a diameter of 0.004 m and a grain length of 0.030 m. The combustion chamber is preceded by a precombustion chamber, which can be considered an extension of the combustion chamber without the fuel around it; this configuration is used in the common rocket application, and also has the purpose of avoiding numerical problems at the grain leading edge. The studied domain is axisymmetrical, thus it can be subdivided only in the axial and radial directions; for the combustion chamber, the domain is divided into 300 subdivisions in the axial direction and 50 in the radial direction. These choices proved to provide a sufficient accuracy for all of the phenomena taking place in the combustion chamber. The solid domain is divided into 300 subdivisions in the axial direction and 25 in the radial, because the grain has a thickness of 0.001 m, which is half of the combustion chamber radius; therefore, the fluid and solid domains are divided in the same way.

The results are presented in the following order. First, the numerical results are compared with the experimental ones obtained at the Space Propulsion Laboratory for the different pressures and mass flow rates; these data are reported by Favarò et al. [10]. In that paper, some numerical data are also available which can be compared with results here in this paper. Finally, a deeper analysis is conducted on some of the variables to investigate their behavior when some operating conditions change, such as pressure, oxygen inlet temperature, and mass flow rate.

Comparison with Experimental Data

The solid fuel regression rate is considered the most important parameter for the hybrid rocket design; therefore, in this work, it is the main parameter investigated. Furthermore, data on the solid fuel regression rate are the only experimental data available from the experiments of Favarò et al. [10] because of the very reliable techniques used to obtain accurate measurements. However, experimentally, it is possible to get only an average regression rate and not the entire regression rate distribution along the grain surface, which is a result available, instead, through the present numerical analysis. To make the comparison, the regression rate distribution is integrated over the entire surface, whereas the regression rate trend along the grain surface is discussed later in this paper.

The experimental analysis showed a slight nonlinear dependency for the regression rate as a function of the pressure and a mass flow rate sensitivity as well. As observed by Risha et al. [9], the regression rate pressure dependency can be related to variable values for the pre-exponential coefficient B_{td} and the activation energy E_{td} in Eq. (47). In this work, the activation energy is taken as a constant ($E_{td} = 11.016\ \text{MJ} \cdot \text{kmol}^{-1}$), because of its slight effect on the solution, and the pressure dependency is addressed only for the pre-exponential coefficient as follows:

$$B_{td} = 2.68821 - 0.00053p - 0.00050p^2\ (\text{mm} \cdot \text{s}^{-1}) \qquad (55)$$

Note that, in this relation, the pressure must be expressed in atm. To reproduce the experimentally observed regression rate pressure sensivity, and to verify if some flow properties are responsible for this particular behavior, a quadratic fitting law has been applied to the experimental data reported in Favarò et al. [10]. This choice has been made because the source of the pressure sensivity in this range is unknown; therefore, the use of another law, such as the linear interpolation of the Risha et al. [9] data, cannot reproduce the observed behavior. Equation (55) shows a monotonic inverse sensitivity with the pressure, with a maximum at 7 atm and a minimum at 16 atm. Therefore, this dependency cannot describe the experimentally observed maximum at 10 atm according to Favarò et al. [10], yielding to disagreement in the regression rate trend with respect to pressure causing underestimations in the regression rate numerical evaluation at 10, 13, and 16 atm. That is, we lose the nonmonotonic regression rate trend with pressure; therefore, regression rates at a pressure higher than 7 atm are underestimated with respect to the experiments.

Table 1 shows the comparison between experimental and numerical average regression rates. Alongside these data, the operating conditions are reported: combustion chamber pressure p, oxygen mass velocity G_{ox}, mass flow rate $\dot{m}$, and Reynolds based on diameter Re_D; the inlet oxygen temperature is always set to 300 K. The numerical results show a good agreement with the experimental results, above all for the pressures of 7, 10, and 13 atm, whereas the difference is larger at 16 atm in the order of 5%. Hence, the numerical solution is considered sufficiently accurate.

Table 1 Comparison between experimental and numerical results for different pressures and oxygen mass velocities, using a quadratic interpolation on pressure based on Favarò et al. data [10] for the pyrolysis law

p, atm	G_{ox}, kg · m^{-2} · s^{-1}	$\dot{m}$, kg · s^{-1}	Re_D	$\bar{\dot{r}}_{exp}$, mm · s^{-1}	$\bar{\dot{r}}_{num}$, mm · s^{-1}
7	150	0.00188	28,958	0.5846	0.5780
10	150	0.00188	28,958	0.5731	0.5786
13	150	0.00188	28,958	0.5577	0.5631
16	150	0.00188	28,958	0.5546	0.5226
7	200	0.00251	38,610	0.6578	0.6522
10	200	0.00251	38,610	0.6583	0.6611
13	200	0.00251	38,610	0.6385	0.6462
16	200	0.00251	38,610	0.6346	0.5992
7	250	0.00314	48,263	0.7499	0.7483
10	250	0.00314	48,263	0.7615	0.7678
13	250	0.00314	48,263	0.7385	0.7442
16	250	0.00314	48,263	0.7269	0.6913
7	300	0.00377	57,915	0.8731	0.8652
10	300	0.00377	57,915	0.9039	0.9085
13	300	0.00377	57,915	0.8808	0.8817
16	300	0.00377	57,915	0.8539	0.8212

Comparison with Numerical Results of Favarò et al. [10]

To make such comparisons, it is worthwhile to analyze the main differences between the models used in the work by Favarò et al. [10] with respect to the models used in this work.

1) In the present work, boundary-layer thickness and flame position are not assumed to have a specific dependency on the axial coordinate, whereas in the Favarò et al. work [10], they were linearly dependent on this variable.

2) The regression rate is not assumed to be uniform alongside the grain surface; the distribution of the regression rate in the axial coordinate is a matter of investigation.

3) No hypotheses have been taken in the present work for the diffusion layers in the fluid and solid; the entire fluid and solid domains are actually solved.

4) In the present work, the hypothesis to have $Pr = Le = Sc = 1$ is maintained, and this is usually a good approximation in the reactive flows.

5) In this paper, velocities are not neglected, but the model is reduced to an axisymmetric problem with only two velocity components that differ from zero.

6) The low Mach number hypothesis is still used; in fact, all of the calculations are used for Mach number values lower than 0.1.

7) Solid fuel grain properties are still considered to be uniform in the radial and axial directions.

8) The fast chemistry assumption is not assumed in this paper; instead, a finite rate chemistry with complex chemical kinetics solution is taken, so that the flame is no longer thin, but becomes thick.

9) No hypotheses are taken for the turbulent viscosity dependency with respect to the axial coordinate.

Despite the availability of the regression rate distribution in this work, comparison with the previous work [10], where only one regression rate value is available because of the monodimensional domain assumption, can be made only for one overall or average regression rate. To make a comparison, it is again necessary to use the average values. However, one must consider that the data for the regression rate in the second part of the Favarò et al. work [10] are taken as input and not as output. Hence, they are coincident with the experimental results, whereas in the present work, they are calculated as output. The analysis is then carried on, analyzing other variables available from both numerical analyses, such as flame temperature, solid fuel surface temperature, and fuel and oxygen mass fractions at the fluid-solid interface.

Table 2 shows the numerical results obtained from the Favarò et al. model [10]. Results obtained in the present work are reported in Table 3.

As far as the flame temperature is concerned, the difference between the obtained values is larger than 1000 K. The adiabatic flame temperature, using this chemical kinetics scheme, is in the range of 3800 to 4000 K, according to the pressure value. Considering that the combustion is fed by pure oxygen, the temperature usually becomes very high, as confirmed by the analyses of Zilliac and Karabeyoglu [11] and Gariani et al. [12]. Such a large difference would be justified by the different evaluations of the heat introduced by combustion. In Favarò et al. [10], the heat amount was assumed as a fixed value, whereas in this work, it is calculated

Table 2 Example of pressure sensitivity of different variables for $G_{ox} = 250\ \text{kg} \cdot \text{m}^{-2} \cdot \text{s}^{-2}$ [10]

p, atm	$\bar{\dot{r}}$, mm · s^{-1}	T_F, K	T_S, K	$Y_{C_4H_6}$	Y_{O_2}
7	0.748	2448.1	983.8	0.774	3.83e − 3
10	0.759	2488.1	984.3	0.774	1.61e − 5
13	0.740	2488.3	1000.3	0.766	4.31e − 5
16	0.726	2488.7	1014.1	0.759	3.91e − 5

Table 3 Pressure-dependent variables used for comparison with the Favarò et al. [10] numerical results for $G_{ox} = 250\ kg \cdot m^{-2} \cdot s^{-1}$

p, atm	$\bar{\dot{r}}$, mm · s^{-1}	T_F, K	T_S, K	$Y_{C_4H_6}$	Y_{O_2}
7	0.748	3524	1047	0.5346	0.0054
10	0.768	3572	1052	0.4578	0.0032
13	0.744	3665	1073	0.4006	0.0027
16	0.691	3697	1097	0.3349	0.0021

according to the chemical kinetics scheme and the thermodynamic conditions. Moreover, the flame temperature does not change in Table 2 when the pressure changes. In the model proposed by Favarò et al. [10], the flame temperature does not change if the regression rate is imposed or if it is not assumed to be pressure dependent. In the solution presented in this paper (Table 3), the flame temperature is instead affected by the pressure, which can be considered both a thermodynamic effect and an effect of the faster chemical kinetics causing a more narrow and higher peak temperature.

Different from the flame temperatures, the surface temperatures are comparable in the two cases. In the first analysis, the surface temperature grows as the pressure increases. The same behavior has been observed in the analysis conducted in the present study. Actually, the surface temperature should reflect the increase in the flame temperature.

Larger differences can be noticed when comparing the fuel and oxygen mass fractions at the fluid-solid interface. In the first case, the fuel appears to be the predominant species at the surface, whereas the oxygen is practically negligible, except in the case with 7 atm. In this analysis, the fuel amount at the surface is lower, and it has the same decreasing behavior as the pressure increases as in the previous case, because obviously a larger pressure means a larger reaction rate. The fuel reduction at the surface is counterbalanced by the increase in the combustion products, which represent the largest amount at the surface. In the second case, the oxygen is a much larger amount than in the first case, with a decreasing trend with respect to pressure.

Parametric Analysis

The parametric analysis can be useful to assess how the main variables in the solution change under different operating conditions. This analysis is conducted by varying the combustion chamber pressure, the inlet oxygen temperature, and the mass flow rate. In fact, as proposed by Risha et al. [9], the solid fuel regression rate can show all of these dependencies, as reported in Eq. (1). This investigation can also be also used to assess the optimal case for the rocket applications.

The results reported hereafter mainly refer to the case previously analyzed for the experimental and numerical comparison. Hence, in this section, other parameters are analyzed, such as the solid fuel regression rate distribution along the grain surface. Also, other properties characteristic of the combustion process and related to the fluid-solid interface are examined, in particular to verify their effect on the regression rate.

The first results reported in the following figures refer to the case with an operating pressure of 10 atm, an oxygen mass velocity of 250 kg · m^{-2} · s^{-2}, and an oxygen inlet temperature of 300 K.

Figure 1 shows the temperature profiles in the fluid flow at different axial positions along the solid grain. Note that the flame temperature is around 3500 K along the entire grain length; however, it increases slightly downstream. Furthermore, the profiles become less and less similar to a cusp. Therefore, the flame becomes thicker downstream; the flame also moves farther from the surface downstream with a near linear increase with respect to the axial coordinate, a condition produced by the hypothesis of equal $Le = Sc = Pr$. The near linear variation in flame standoff distance is related to near linear growth in boundary-layer thickness. The approximation by Favarò et al. [10] concerning linear growth rates for boundary-layer thickness and flame standoff distance was very reasonable.

Another interesting parameter, shown in Fig. 2, is the axial velocity profile. The axial velocity at the inlet is fixed to 19.5 m · s^{-1} according to the imposed mass flow rate. Note that, different from a nonreacting boundary layer, the velocity profile is not monotonic, but it reaches a maximum in the flame position in the radial direction for any axial location. Both the maximum and the freestream velocities increase in the downstream direction, reaching values larger than 8 and 3 times the inlet velocity, respectively. In all cases, the axial component of the velocity is zero at the wall because of the no-slip condition. The boundary-layer displacement results in an acceleration of the freestream because streamlines are constrained due to the boundary-layer displacement thickness. A pressure gradient results in the core flow, which also causes an acceleration of the boundary-layer gases. The less dense gases near the flame accelerate more.

Other important parameters that one should analyze are the species mass fractions for oxygen, fuel, and combustion products. Figure 3 plots the oxygen mass fractions at different axial locations. As said, pure oxygen is injected at the combustion chamber inlet, so the freestream is represented by pure oxygen, too. All profiles show a large gradient where the flame is located moving from a value equal to 1 in the freestream to values close to 0 below the flame and at the fluid-solid interface. Therefore, only a small amount of oxygen can cross the flame without reacting, and can enhance the pyrolysis process.

Figure 4 depicts the fuel mass fraction in different axial locations. This substance is produced by the fuel pyrolysis. Therefore, it is obvious that it is not present in the freestream, but its concentration decreases quite sharply moving from the surface to the flame. Its concentration gradient is smaller downstream because the flame is farther from the surface, and because there is also an accumulation of

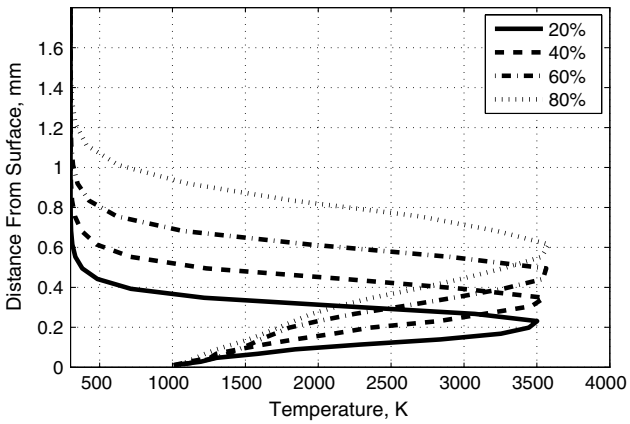

Fig. 1 Temperature (Kelvins) profiles at different axial locations for the case with $p = 10$ atm and $G_{ox} = 250\ kg \cdot m^{-2} \cdot s^{-1}$.

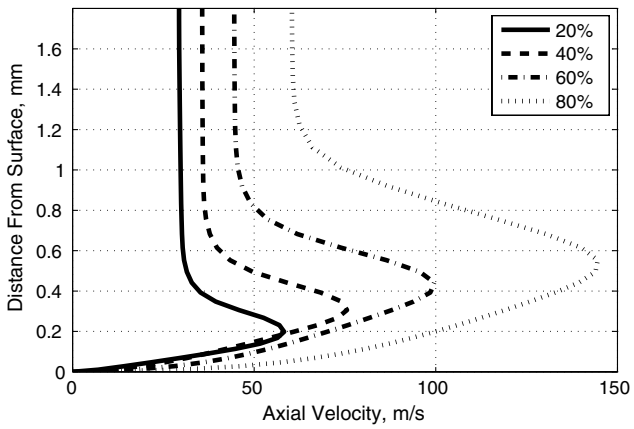

Fig. 2 Axial velocity (m · s^{-1}) profiles at different axial locations for the case with $p = 10$ atm and $G_{ox} = 250\ kg \cdot m^{-2} \cdot s^{-1}$.

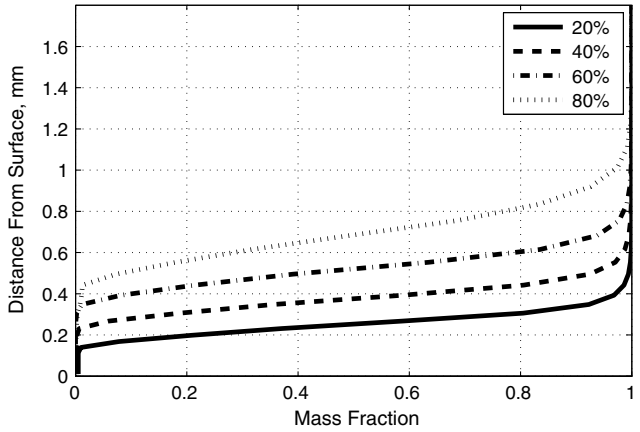

Fig. 3 Oxygen mass fraction profiles at different axial locations for the case with $p = 10$ atm and $G_{ox} = 250\ \mathrm{kg \cdot m^{-2} \cdot s^{-1}}$.

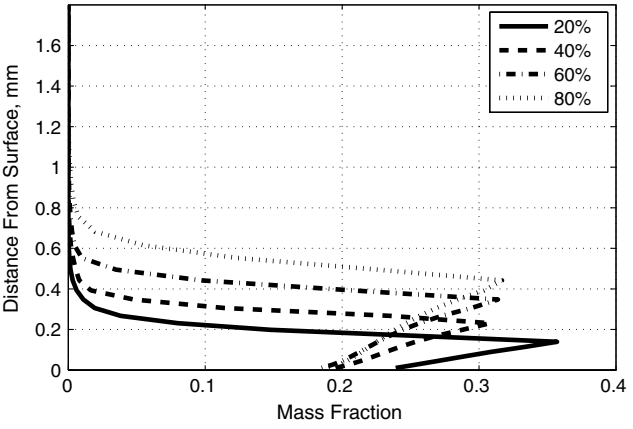

Fig. 5 CO mass fraction profiles at different axial locations for the case with $p = 10$ atm and $G_{ox} = 250\ \mathrm{kg \cdot m^{-2} \cdot s^{-1}}$.

the unburnt fuel coming from upstream locations. Note that the value at the surface is not equal to 1 because the used boundary conditions allow the other substances to reach the surface.

Figure 5 shows the mass fraction for carbon monoxide (CO), one of the most important intermediate combustion products. Note that there is a great difference in the profiles at the first reported axial location with respect to the others, in terms of both the maximum value in the flow and the value at the surface. Because CO is an intermediate combustion product, it is the first combustion product largely produced upstream; then, it is consumed to produce the final combustion products such as CO_2 and H_2O. This is why the amount of CO is very large upstream and decreases downstream. Then, its maximum value does not change so much downstream because there is only a fixed amount that is converted in other species. The very slight increase downstream can be caused by the slightly reduced conversion in CO_2; actually, downstream the flame becomes thicker, so the standoff distance of the flame zone, where H_2O and CO are mainly produced, increases, and the reduction in the concentration causes the slightly lower conversion rate to CO_2; therefore, CO concentration increases slightly with increasing downstream distance because it is not converted at the same rate as upstream. Therefore, the CO mass fraction can also be considered a parameter to assess the combustion efficiency.

As far as the final combustion products are concerned, Fig. 6 plots the mass fractions for the carbon dioxide (CO_2). CO_2 is produced by the destruction of CO; therefore, they usually have opposite trends. Actually, the amount of CO_2 is smaller upstream and grows downstream because of the CO consumption. Downstream, its maximum value does not change so much, but its overall amount in the flame increases considering that the profiles enlarge, as does its amount at the surface.

Figure 7 depicts the water mass fractions in different axial locations. The water amount shows decreases in the maximum value in the flame and at the surface moving downstream. This can be explained taking into account the second reaction of the chemical kinetics scheme [see Eq. (28), where the H_2O is a reactant that produces CO_2 along with CO). Therefore, a certain amount of water is destroyed to produce the other final combustion product. Downstream, water production is reduced because oxygen, coming from the freestream, and hydrogen, coming from the fuel, are mainly located in opposite positions with respect to the flame location, reducing their reaction amount.

Pressure Sensitivity

The regression rate pressure dependency is one focus of this work. In particular, the assessment of the parameters that affect the behavior of the regression rate would be useful in understanding how to increase its value, which is very small in the hybrid rockets. Operating pressure can act on the regression rate directly, through Eqs. (47) and (55), or indirectly on either combustion or fluid-solid interface parameters. The accuracy in the regression rate reproduction is good using the quadratic fitting law; a maximum error in terms of $\pm 5\%$ is expected. The cases reported hereafter are the cases previously analyzed for comparison with the experimental and numerical results. In this analysis, it is noteworthy that a change in the operating pressure also changes the gas density, through the perfect gas law, and then can also change the mass flow rate:

$$\rho = \frac{p}{RT} \qquad \dot{m} = \rho u_{\mathrm{in}} S \tag{56}$$

Because the geometrical characteristics do not change, it is necessary to vary the oxygen inlet velocity in an opposite fashion to the pressure

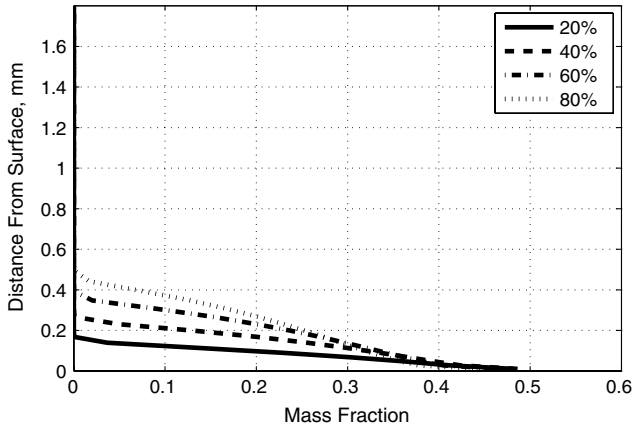

Fig. 4 Fuel mass fraction profiles at different axial locations for the case with $p = 10$ atm and $G_{ox} = 250\ \mathrm{kg \cdot m^{-2} \cdot s^{-1}}$.

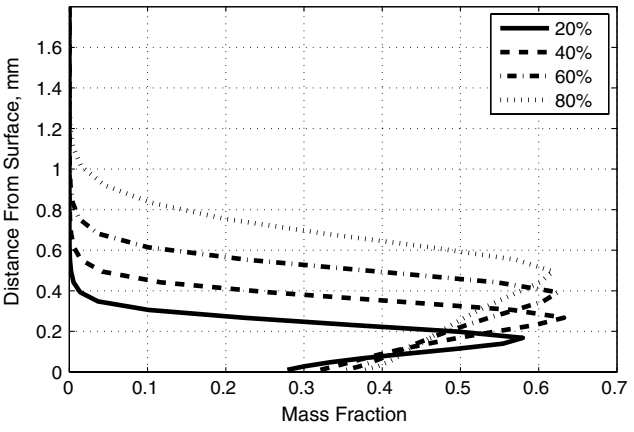

Fig. 6 CO_2 mass fraction profiles at different axial locations for the case with $p = 10$ atm and $G_{ox} = 250\ \mathrm{kg \cdot m^{-2} \cdot s^{-1}}$.

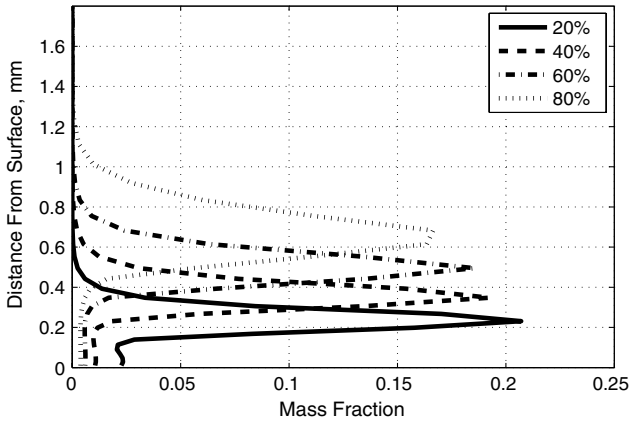

Fig. 7 H_2O mass fraction profiles at different axial locations for the case with $p = 10$ atm and $G_{ox} = 250$ kg · m^{-2} · s^{-1}.

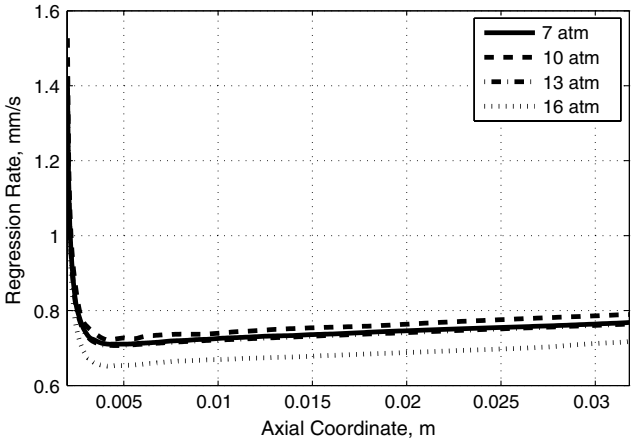

Fig. 8 Solid grain regression rate (mm · s^{-1}) for different pressures.

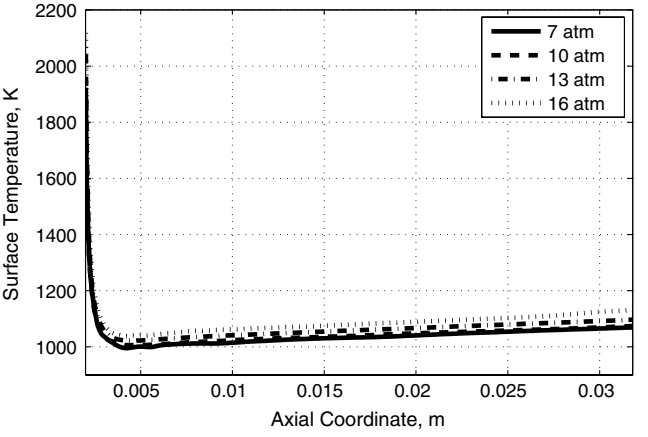

Fig. 9 Solid grain surface temperature (Kelvins) for different pressures.

to maintain a fixed mass flow rate between the different computations. This consideration is needed if one wants to isolate the pressure influence on the solution.

Table 4 reports some of the most important initial data used for each of the computations. As previously stated, the condition of equal oxygen inlet temperatures and mass flow rates has been realized.

Table 5 reports some of the results previously presented in Figs. 1–7. For this parametric analysis, it does not appear useful to show again the pictures with the flame temperature and combustion product mass fractions along the axial direction, because the trends are very similar. Therefore, in Table 5, we only present their maximum values in the flame when pressure changes to assess its effect on them. The flame temperature increases as the pressure increases, which is common in combustion. The intermediate combustion product CO decreases when pressure increases, whereas the final combustion products CO_2 and H_2O increase, so the combustion is more efficient.

Regression rate profiles with different pressures are shown in Fig. 8. The average values have already been analyzed in the experimental and numerical comparisons. From this figure, one can also observe the regression rate trend along the entire grain length; the general trend does not appear to be very affected by pressure. However, note the peak regression rate at the grain leading edge, which is due to the large heat exchange, because it is the location where the flame is closer to the surface. The regression rate then drops sharply in the downstream direction, reaching a minimum not far from the leading edge. The regression rate then slightly increases downstream, mainly due to the improved local heat transfer through an increase in the local flame temperature, a behavior also found in the analysis by Gariani et al. [12].

Table 4 Initial conditions for pressure sensitivity analysis

p, atm	$\dot{m}$, kg · s^{-1}	T_{in}, K	μ_{in}, m · s^{-1}	Re_D	Re_L
7	0.00314	300	27.815	48,263	361,973
10	0.00314	300	19.470	48,263	361,973
13	0.00314	300	14.977	48,263	361,973
16	0.00314	300	12.169	48,263	361,973

Table 5 Comparison between flame temperature and combustion product mass fractions for different pressures

p, atm	T_F, K	Y_{CO}	Y_{CO_2}	Y_{H_2O}
7	3524	0.565	0.452	0.173
10	3572	0.530	0.569	0.190
13	3665	0.516	0.642	0.191
16	3697	0.421	0.717	0.305

A main driver for the regression rate would be the solid surface temperature at which pyrolysis takes place. In fact, note that the trend in Fig. 9 along the grain length is very similar, with the peak surface temperature at the leading edge and the sharp decrease followed by a slight increase moving downstream. However, although surface temperature appears to describe the trend, it does not agree with the maximum values; in fact, the surface temperature increases as the pressure increases, whereas a different behavior has been encountered for the regression rate. This means that the change in regression rate is driven by something beyond the heating of the solid fuel when a large change in the pressure levels occurs.

The role of oxygen has been conjectured to be very important in the pyrolysis process. For this reason, the oxygen mass fraction behavior at the fluid-solid interface with respect to pressure is reported in Fig. 10. Note that the oxygen amount at the surface is very low, with peaks at the grain leading edge. However, one can observe a general decrease in its amount when the pressure decreases as well. This can confirm that oxygen can play a role in the enhancement of the pyrolysis phenomenon when the pressure is lower, as suggested by Risha et al. [9].

Oxygen Inlet Temperature Sensitivity

The oxygen inlet temperature sensitivity has been suggested by the empirical correlation proposed by Risha et al. [9] [see Eq. (1)]. In this analysis, this dependency can be easily assessed; the previously reported results have been obtained for an oxygen inlet temperature of 300 K, to be comparable with experimental results. However, to ignite the fuel-oxygen mixture, in the numerical computations, it is necessary to provide a sufficient oxygen inlet temperature to allow the reactions to take place in a significant way. Therefore, the oxygen inlet temperature has been initially set to 900 K and then dropped to

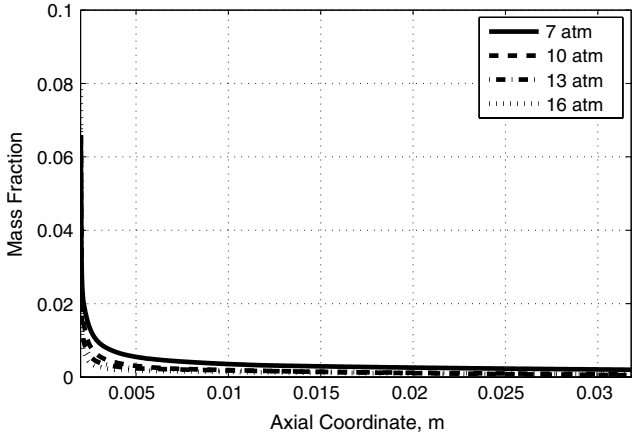

Fig. 10 Oxygen mass fraction at the fluid-solid interface for different pressures.

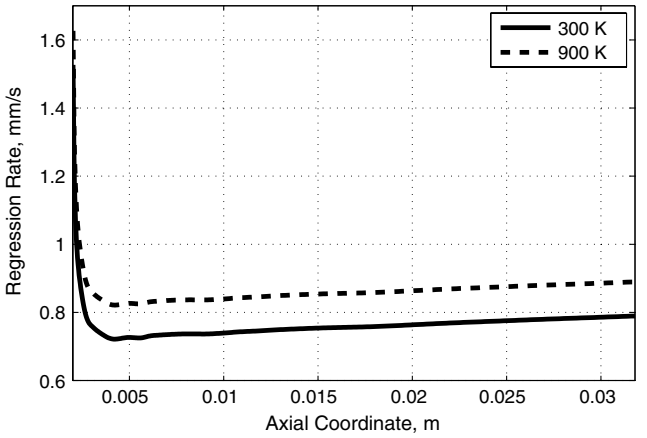

Fig. 11 Solid grain regression rate ($mm \cdot s^{-1}$) for different oxygen inlet temperatures.

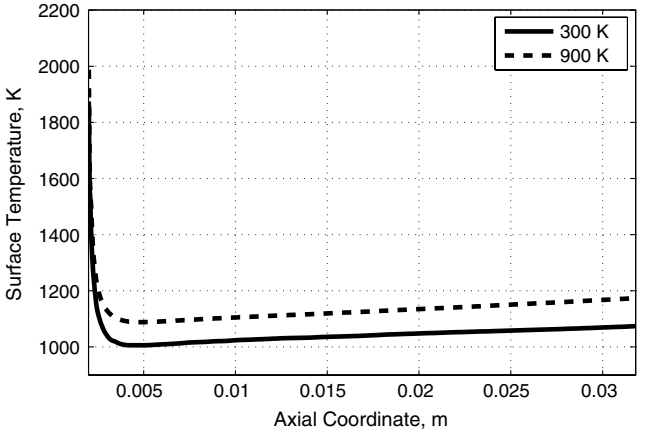

Fig. 12 Solid grain surface temperature (Kelvins) for different oxygen inlet temperatures.

300 K, where it is held steady. This sensitivity analysis will take into consideration these two oxygen inlet temperatures. The case analyzed is the same reported in this work and uses the data reported in Table 6.

To isolate the oxygen inlet temperature dependency, it is necessary to maintain the same operating conditions, in particular, the mass flow rate, which changes according to Eq. (56). Therefore, the oxygen inlet velocity is increased by 3 times the value at a lower temperature. However, the Reynolds numbers are lower because viscosity also nonlinearly changes with temperature.

Table 7 reports the comparison between the main flame properties for different oxygen inlet temperatures. As far as the flame temperature is concerned, the decrease in the inlet temperature causes a reduction of approximately 100 K. This reduction for a lower inlet temperature can be due to the colder oxygen molecules that feed the flame and to the enhanced thermal exchange through diffusion that subtracts heat from the flame. As stated, density increases if inlet temperature decreases, which causes a larger number of collisions, and then a larger number of reactions. The concentrations of intermediate combustion product CO are actually lower, whereas the final combustion product concentrations, i.e., CO_2 and H_2O, are higher.

Figure 11 depicts the regression rate distribution for the two cases. The oxygen inlet temperature does not appear to modify the regression rate distribution curve shape very much. Rather, it modifies the average and local values; in fact, regression rate appears to be higher by approximately $0.1\ mm \cdot s^{-1}$ in the hot case approximately everywhere along the surface length.

The main driver in this case appears to be the grain surface temperature (see Fig. 12). It affects not only the regression rate distribution, but its value as well. A difference of less than 100 K can be noted, similar to the difference observed for the flame temperature. Therefore, the higher flame temperature enhances the thermal exchange at the fluid-solid interface, and because these cases are solved with the same pressure, the oxygen inlet temperature influence becomes dominant.

Figure 13 shows the oxygen amount at the fluid-solid interface in the two analyzed cases. The difference is very small; however, there is more oxygen in the hotter case. This can be explained by the small displacement of the flame upstream toward the inflow for the lower inlet temperature, which is due to the higher gas density and lower velocity when the temperature is decreased; the residence time increases and the flame displaces. The oxygen reduction can also be considered one of the parameters that affects the regression rate decrease observed for the lower inlet temperature.

Table 6 Initial conditions for oxygen inlet temperature dependency analysis

p, atm	$\dot{m}$, $kg \cdot s^{-1}$	T_{in}, K	μ_{in}, $m \cdot s^{-1}$	Re_D	Re_L
10	0.00314	300	19.470	48,263	361,973
10	0.00314	900	58.410	22,361	167,710

Table 7 Comparison between flame temperature and combustion product mass fractions for different oxygen inlet temperatures

T_{in}, K	T_F, K	Y_{CO}	Y_{CO_2}	Y_{H_2O}
300	3572	0.530	0.569	0.190
900	3664	0.562	0.527	0.187

Mass Flow Rate Sensitivity

Experimental activities showed how sensitivity to mass flow rate is fundamental in the correct regression rate determination. This observation is true for the experimental data previously compared, but there are many examples in the literature showing a direct dependency between mass flow rate $\dot{m}$ (or oxygen mass velocity G_{ox}) and the average regression rate, starting from the studies by Marxman and Wooldridge [3] and Marxman and Gilbert [4].

The cases must be studied at the same oxygen inlet temperature and operating pressure to isolate the mass flow rate dependency on the analyzed parameters.

Because geometrical characteristics are fixed, the only way to change the mass flow is to vary the oxygen inlet velocity. In this case, density does not change because pressure and temperature are the same for each case; therefore, it is sufficient to change the velocity according to the increment one wants to obtain on the mass flow. Table 8 reports the main data for the computations.

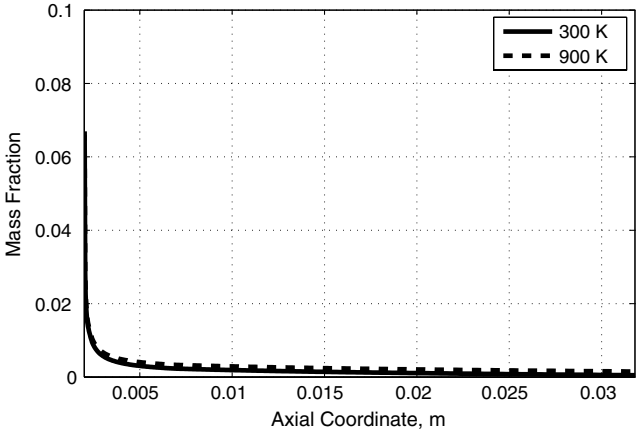

Fig. 13 Oxygen mass fraction at the fluid-solid interface for different oxygen inlet temperatures.

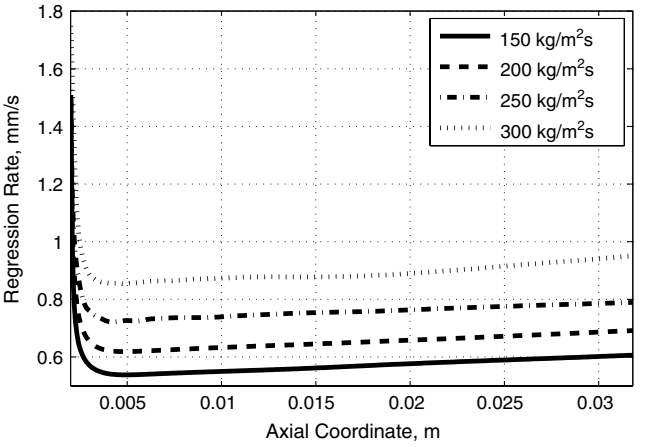

Fig. 14 Solid grain regression rate ($mm \cdot s^{-1}$) for mass flow rates.

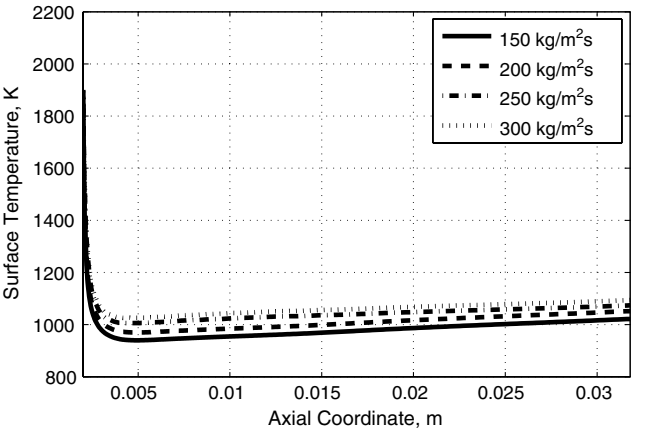

Fig. 15 Solid grain surface temperature (Kelvins) for different mass flow rates.

Table 9 reports the main results related to the flame when mass flow rate is changed. The mixture ratio O/F between the oxygen mass inflow rate ($\dot{m}$) and the fuel mass gasification rate ($\rho_s \dot{r} A_b$) is also reported. The flame temperature decreases as the mass flow rate is increased. The explanation may be that the species are transported faster toward the combustion chamber end, so the residence times become very small. Also, the flame is forced closer to the surface at higher flow rates, resulting in greater heat loss to the solid. Note also the slight increases in CO and decreases in CO_2 and H_2O as the mass flow rate increases; again, the explanation may be as previously stated: that there is less time for complete reactions, so the combustion becomes more inefficient.

Figure 14 shows the regression rate distribution for the four analyzed cases. One can immediately note the large difference in average and local values for the different mass flow rates, a difference that is larger than that obtained with different pressures; the difference between the maximum and minimum case can be assessed in a reduction of approximately 40%. Moreover, the mass flow rate dependency is monotonic, whereas the pressure one was more complicated. Again, the trends are not so different case by case, because the surface temperature is still their main driver.

Solid surface temperature is depicted in Fig. 15. The temperature increases as the mass flow rate increases in a range of approximately 100 K between the maximum and minimum. Hence, temperature is the main driver for the regression rate trend and values; however, as reported in Table 9, the flame temperature is lower when the mass flow rate increases, whereas the surface temperature is higher. This is explained by the flame position, which becomes closer to the surface because the larger amount of mass injected at the inflow pushes the flame toward the surface, so that the thermal exchange between the flame and fluid-solid interface is enhanced.

Table 8 Initial conditions for mass flow rate sensitivity analysis

G_{ox}, $kg \cdot m^{-2} \cdot s^{-1}$	$\dot{m}$, $kg \cdot s^{-1}$	p, atm	T_{in}, K	μ_{in}, $m \cdot s^{-1}$	Re_D	Re_L
150	0.00188	10	300	11.682	28,958	217,185
200	0.00251	10	300	15.576	38,610	289,575
250	0.00314	10	300	19.470	48,263	361,973
300	0.00377	10	300	23.364	57,915	434,363

Table 9 Comparison between flame temperature and combustion product mass fractions for different mass flow rates

G_{ox}, $kg \cdot m^{-2} \cdot s^{-1}$	O/F	T_F, K	Y_{CO}	Y_{CO_2}	Y_{H_2O}
150	9.42	3642	0.505	0.595	0.195
200	11.01	3603	0.521	0.582	0.192
250	11.86	3572	0.530	0.569	0.190
300	12.03	3548	0.539	0.550	0.189

Figure 16 shows the oxygen mass fraction at the fluid-solid interface for the four cases. For most of the grain length, the difference can be neglected. Only at the grain leading edge can one note a slight difference; in fact, the oxygen diminishes as the mass flow rate is reduced. The increment for the larger mass flow rate cases is due to the reduced combustion efficiency that converts less oxygen; hence, more oxygen can cross the flame and reach the surface. Downstream the differences become negligible because the flame is closer to the surface, and oxygen can react more in the flame zone with less diffusion below the flame.

Finally, Fig. 17 shows the regression rate behavior with respect to G_{ox} for the numerical calculations. A fitting law is applied to these data to find a power law that correlates the regression rate value to the oxygen mass velocity:

$$\dot{r} = 0.0935 G_{ox}^{0.65} \tag{57}$$

where $\dot{r}$ is expressed in $mm \cdot s^{-1}$ and G_{ox} in $g \cdot cm^{-2} \cdot s^{-1}$. The G_{ox} exponent is located between the values proposed by the analysis by Marxman and Wooldridge [3], which was 0.8, and the analysis by Risha et al. [9], which was 0.5.

Comparison Between Turbulence Models

All results presented so far have been obtained using the k-ϵ model to close the turbulence problem. However, a second model, including the variance of the scalar quantity related to mixture fraction, has been developed. To make a comparison between the two models, it was necessary to make a computation with the same physical parameters as the case previously calculated with the k-ϵ model only. The compared case has an operating pressure of 10 atm, with an oxygen

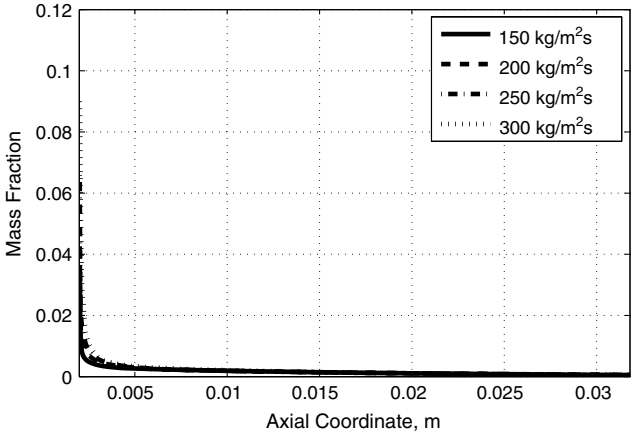

Fig. 16 Oxygen mass fraction at the fluid-solid interface for different mass flow rates.

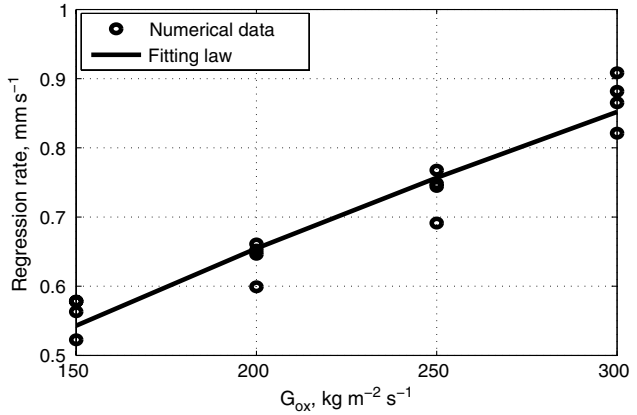

Fig. 17 Regression rate vs G_{ox}: numerical data and fitting law.

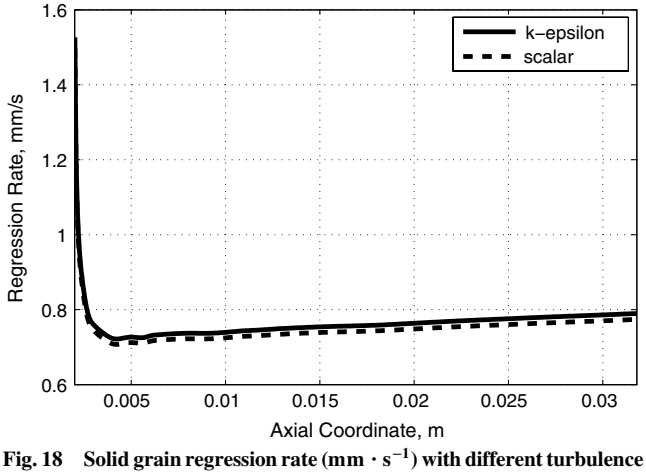

Fig. 18 Solid grain regression rate (mm · s^{-1}) with different turbulence models.

mass velocity of 250 kg · m^{-2} · s^{-1} and an oxygen inlet temperature set to 300 K.

The differences in the results between the two models are very small (see Table 10).

Table 10 Flow properties comparison between the case with momentum mixing time and the one with scalar mixing time

	T_F, K	Y_{CO}	Y_{CO_2}	Y_{H_2O}
k-ϵ	3572	0.530	0.569	0.190
Scalar	3573	0.527	0.578	0.198

As far as the flame temperature is concerned, no significant changes can be evaluated using one turbulence model or the other. The combustion products species mass fractions show, instead, a different behavior. Actually, the amount of CO is smaller in the scalar case, whereas the final combustion products amount, i.e., CO_2 and H_2O, shows a significant increase.

Figure 18 depicts the regression rate comparison when the k-ϵ model or the scalar variance model (scalar) is used. Note that the difference is very slight: the scalar case shows a regression rate that is a little lower with respect to the k-ϵ case, whereas the distribution is not very affected.

Conclusions

Numerical simulations of the combustion chamber ballistic of a hybrid rocket motor have been performed, and all analytical tools used for that task have been explained. In summary, the regression rate was found to increase monotonically with pressure up to 10 atm, beyond which a monotonic decrease was calculated. Yet, surface temperature monotonically increased throughout the studied pressure range. Both regression rate and surface temperature increased with both oxygen inlet temperature and oxygen mass flow rate. Two different turbulence models showed little difference.

The behaviors of the solid fuel regression rate and other characteristic properties have been investigated under different operating conditions. The numerical analysis provided data that cannot usually be found easily through experiments, such as the regression rate distribution along the grain surface, which is highly variable in this coordinate. Regression rate has also been studied under different pressures, oxygen inlet temperatures, and mass flow rates.

In agreement with experiments, the numerical analysis provided a very complex regression rate pressure sensitivity. This behavior is strictly related to the pressure-dependent pre-exponential coefficient and to the solid surface temperature. The oxygen concentration at the fluid-solid interface is related to pressure; it is larger for lower pressure, confirming the analysis in which the oxygen below the flame was proposed to be a factor in the pyrolysis enhancement. However, in the experimental data of confirmed that the regression rate was very dependent on mass flow rate.

The analysis with variable oxygen inlet temperature showed the large influence of the solid surface temperature on the regression rate value, when pressure and mass flow rate are constant. Also, the oxygen diminution appeared to be a factor in the lower regression rate at lower temperatures.

In the last analysis, the regression rate was confirmed to be very dependent on mass flow rate. Again, in this case, an increase in the oxygen amount below the flame is observed when the regression rate is higher.

With this numerical analysis, the regression rate sensitivities with respect to each of the investigated parameters have been assessed; therefore, the observations made are confirmed, and the regression rate is dependent on each of these parameters.

Acknowledgment

Professor Said Elghobashi provided valuable suggestions for the treatment of turbulent fluctuation correlations.

References

[1] Biblarz, O., and Sutton, G. P., *Rocket Propulsion Elements*, Wiley, New York, 2001, pp. 579–606.

[2] Karabeyoglu, M. A., Cantwell, B. J., and Altman, D., "Development and Testing of Paraffin-based Hybrid Rocket Fuels," *37th AIAA/American Society of Mechanical Engineers/Society of Automotive Engineers/ American Society for Engineering Education Joint Propulsion Conference and Exhibit*, AIAA Paper 2001-4503, 2001.

[3] Marxman, G. A., and Wooldridge, C. E., "Fundamentals of Hybrid Boundary Layer Combustion," *Heterogeneous Combustion Conference*, AIAA Paper 1963-505, 1963.

[4] Marxman, G. A., and Gilbert, M., "Turbulent Boundary Layer Combustion in the Hybrid Rocket," *9th International Symposium on Combustion*, Elsevier, New York, 1963, pp. 371–383.

[5] Price, C. F., and Smoot, L. D., "The Pressure Dependence of Hybrid Fuel Regression Rates," *AIAA Journal*, Vol. 5, No. 1, 1967, pp. 102–106. doi:10.2514/3.3914

[6] Price, C. F., and Smoot, L. D., "Regression Rate Mechanism of Nonmetalized Hybrid Fuel Systems," *2nd Aerospace Science Meeting*, AIAA Paper 1965-56, 1965.

[7] Arisawa, H., and Brill, T. B., "Flash Pyrolysis of Hydroxyl-Terminated Polybutadiene (HTPB) I: Analysis and Implications of the Gaseous Products," *Combustion and Flame*, Vol. 106, Nos. 1–2, 1996, pp. 131–143. doi:10.1016/0010-2180(96)00253-2

[8] Arisawa, H., and Brill, T. B., "Flash Pyrolysis of HTPB II: Implications of the Kinetics to Combustion of Organic Polymers," *Combustion and Flame*, Vol. 106, Nos. 1–2, 1996, pp. 144–154. doi:10.1016/0010-2180(95)00254-5

[9] Risha, G. A., Harting, G. C., Kuo, K. K., Peretz, A., Joch, D. E., Jones, H. S., and Arves, J. P., "Pyrolysis and Combustion of Solid Fuels in Various Oxidizing Environments," *34th AIAA/American Society of Mechanical Engineers/Society of Automotive Engineers/American Society for Engineering Education Joint Propulsion Conference and Exhibit*, AIAA Paper 1998-3184, 1998.

[10] Favarò, F. M., Sirignano, W. A., Manzoni, M., and DeLuca, L. T., "Solid Fuel Regression Rate Modeling for Hybrid Rockets," *Journal of Propulsion and Power*, Vol. 29, No. 1, 2013, pp. 205–215. doi:10.2514/1.B34513

[11] Zilliac, G., and Karabeyoglu, M. A., "Hybrids Rocket Fuel Regression Rate Data and Modeling," *42nd AIAA/American Society of Mechanical Engineers/Society of Automotive Engineers/American Society for Engineering Education Joint Propulsion Conference and Exhibit*, AIAA Paper 2006-4504, 2006.

[12] Gariani, G., Maggi, F., and Galfetti, L., "Numerical Simulation of HTPB Combustion in a 2D Hybrid Slab Combustor," *Acta Astronautica*, Vol. 69, Nos. 5–6, 2011, pp. 289–296. doi:10.1016/j.actaastro.2011.03.015

[13] OpenFOAM Foundation, "The Open Source CFD Toolbox," TR, http://www.openfoam.org/docs/user, 2012.

[14] Kuo, K. K., *Principles of Combustion*, Wiley-Interscience, New York, 1986, pp. 161–227.

[15] Elghobashi, S. E., and Launder, B. E., "Turbulent Time Scales and The Dissipation Rate of Temperature Variance in the Thermal Mixing Layer," *Physics of Fluids*, Vol. 26, No. 9, 1983, pp. 2415–2419. doi:10.1063/1.864426

[16] Jones, P. W., and Whitelaw, J. W., "Calculation Methods for Reacting Turbulent Flows: A Review," *Combustion and Flame*, Vol. 48, No. 1, 1982, pp. 1–26. doi:10.1016/0010-2180(82)90112-2

[17] Granata, S., Faravelli, T., and Ranzi, E., "Kinetic Modeling of Counterflow Diffusion Flames of Butadiene," *Combustion and Flame*, Vol. 131, No. 3, 2002, pp. 273–284. doi:10.1016/S0010-2180(02)00407-8

[18] Goldaniga, A., Faravelli, T., and Ranzi, E., "The Kinetic Modeling of Soot Precursors in a Butadiene Flame," *Combustion and Flame*, Vol. 122, No. 3, 2000, pp. 350–358. doi:10.1016/S0010-2180(00)00138-3

[19] Golovitchev, V. I., Bergman, M., and Montorsi, L., "CFD Modeling of Diesel Oil and DME Performance in a Two-stroke Free Piston Engine," *Combustion Science and Technology*, Vol. 179, Nos. 1–2, 2007, pp. 417–436. doi:10.1080/00102200600837242

[20] Golovitchev, V. I., Nordin, N., Jarnicki, R., and Chomiak, J., "3-D Diesel Spray Simulations Using a New Detailed Chemistry Turbulent Combustion Model," *Coordinating European Council/Society of Automotive Engineers (SAE) Spring Fuels and Lubricant Meeting*, SAE Technical Paper 2000-01-1981, June 2000.

[21] Karrholm, F. P., "Numerical Modelling of Diesel Spray Injection, Turbulence Interaction and Combustion," Ph.D. Thesis, Chalmers Univ. of Technology, Goteborg, Sweden, 2008.

[22] Siegel, R., and Howell, J. R., *Thermal Radiation Heat Transfer*, Hemisphere Publishing Corp., Washington, DC, 1992, pp. 663–697.

[23] Sazhin, S. S., Sazhina, E. M., Faltsi-Saravelou, O., and Wild, P., "The P-1 Model for Thermal Radiation Transfer: Advantages and Limitations," *Fuel*, Vol. 75, No. 3, 1996, pp. 289–294. doi:10.1016/0016-2361(95)00269-3

[24] Ramohalli, K. N., and Yi, J., "Hybrids Revisited," *26th AIAA/American Society of Mechanical Engineers/Society of Automotive Engineers/American Society for Engineering Education Joint Propulsion Conference and Exhibit*, AIAA Paper 1990-1962, 1990.

J. Oefelein
Associate Editor